electronics

MDPI

Communication

Design of a Compact Microstrip Decoupled Array

Zibin Weng, Dan Yang * and Kaibin Xue

Key Laboratory of Antennas and Microwave Technology, Xidian University, Xi'an 710071, China; zibinweng@mail.xidian.edu.cn (Z.W.); kbxue@stu.xidian.edu.cn (K.X.)
* Correspondence: 22021211292@stu.xidian.edu.cn; Tel.: +86-3992015043

Abstract: A one-dimensional mono-pulse microstrip antenna plays an important role in target detection, tracking, recognition and imaging. However, feeding and coupling are the main reasons for the large size of the mono-pulse antenna, which is not conducive to miniaturization and integration. A miniaturized mono-pulse antenna is proposed to reduce the size and improve the integration in antenna design. The proposed antenna has a more compact size and good isolation, with a well-maintained radiation pattern and zero depth. The antenna unit size is 0.19 $\lambda_0 \times 0.19\ \lambda_0 \times 0.006\ \lambda_0$. The overall antenna size is 78 mm × 78 mm × 1.48 mm (0.63 $\lambda_0 \times 0.63\ \lambda_0 \times 0.0012\ \lambda_0$). In this communication, a general decoupling feeding network for two-element microstrip array antennas is also designed. Experiment validations confirm that the operating frequency of the designed antenna system is at 2.45 GHz with a gain of 5.54 dBi. The return loss of the sum and difference ports is 16.14 dB and 15.2 dB, respectively. The isolation of the ports is 36.6 dB. The proposed miniaturized mono-pulse antenna is approximately 64% smaller in size compared to previous versions.

Keywords: array antenna; miniaturization; decoupling network; microstrip antenna

check for updates

Citation: Weng, Z.; Yang, D.; Xue, K. Design of a Compact Microstrip Decoupled Array. *Electronics* **2023**, *12*, 4163. https://doi.org/10.3390/electronics12194163

Academic Editors: Giovanni Crupi and Matteo Bruno Lodi

Received: 28 August 2023
Revised: 27 September 2023
Accepted: 4 October 2023
Published: 7 October 2023

1. Introduction

With the rapid advancement of wireless communication systems and radar technologies [1], the demand for compact and high-performance antennas has grown exponentially. Conventional antennas have become impractical due to their size, weight, power consumption, and limited flexibility. In response to this need, miniaturized mono-pulse antennas have emerged as a great solution, offering a compact dimension factor while maintaining excellent performance.

A one-dimensional miniaturized mono-pulse antenna is suggested in this research. It is smaller than typical designs but still retains good radiation patterns. By minimizing the antenna's physical dimensions and array spacing, the proposed antenna achieves miniaturization. However, coupling is inevitable as antenna spacing is shrunk. As a result, the antenna's performance degrades and its radiation efficiency decreases. Therefore, to achieve the decoupling function, the feed network needs to be upgraded.

Researchers have focused on various decoupling methods to reduce antenna coupling. In [2], a technique of decoupling dielectric stubs (DDS) [3] was applied to a 4 × 4 dual-polarized and wideband antenna array. The DDS can achieve all port-to-port isolations over 25 dB from 4.4 to 5.0 GHz for all the coupling paths, which are 7 dB higher than their counterparts without the DDS. In [4], the neutralization line [5] is used to design a UWB MIMO antenna that covers the 3.1–5 GHz band with isolation greater than 22 dB. In [6], a tunable decoupling and matching network [7,8] (DMN) for a two-element closely spaced antenna array is presented. It uses only one varactor to achieve a tuning range of 18.8% with both return loss and isolation better than 10 dB. In [9], a self-decoupling structure was designed to present a new decoupling concept for dual-band shared-aperture base station antenna arrays. This approach provides the antenna array with both in-band and in-band decoupling capabilities. The co-polarized in-band coupling between the designed high-band antennas is reduced by about 9 dB to 26.9 dB. In [10], a new decoupling

method for phased array antenna units is proposed. The decoupling of the antenna units is achieved by embedding non-radiating coupled resonators between the antenna units. A mutual coupling reduction of more than 10 dB is achieved over the entire operating bandwidth. A decoupling method for slit antenna arrays is proposed in [11]. The array antenna decoupling surface consists of partially reflective metal patches. In [12], a quadratic slit antenna array based on ADS is simulated, and the mutual coupling is less than −15 dB over the impedance bandwidth of 2.35–2.545 GHz.

Microstrip antennas can be miniaturized by slotting the antenna surface or ground plane or by loading shorting probes. In [13], Jianxing Li et al. proposed a compact circularly polarized microstrip antenna with square-ring slots and loaded shorting probes [14]. The overall size is 0.33 λ × 0.33 λ × 0.04 λ with a 3 dB measured gain. In [15], the antenna achieved high gain by incorporating a shorted probe loaded with a strip line. The antenna has dimensions of 0.57 λ × 0.57 λ × 0.09 λ and achieves a high gain of 8.5 dBi. In [16], a defected ground structure (DGS) [17] was used to design a small decoupled MIMO antenna array. It etches cross slots on a metal ground plane to alter the distributed capacitance and inductance of the transmission lines, achieving decoupling. The dimensions of the designed antenna unit are 0.23 λ × 0.27 λ × 0.0058λ, and the isolation at 5.8 GHz is greater than 20 dB. In [18], a compact CPMA was designed with the use of an artificial magneto-dielectric material [19]. The antenna has an overall size of 0.303 λ × 0.303 λ × 0.01 λ with a measured peak gain of −3.75 dBic over the frequency band [20]. These methods generally result in a size reduction of about 30–50%.

The antenna unit designed in this paper was miniaturized using the surface slotting technique. The size of the antenna unit is greatly reduced by combining slots from different structures. By means of formula derivation, the suggested decoupling network for a two-element array is generalized, and any two-element antenna array can be decoupled. The miniaturization of the decoupling network is realized using the equivalent circuit. The final-designed mono-pulse antenna is compact while maintaining the shape of the radiation pattern and maximizing the gain.

2. Materials and Methods

2.1. Antenna Configuration

Two aspects are considered in the miniaturization design of a two-element microstrip patch array. The patch can be miniaturized by means of the slotting method, and the antenna size can be significantly reduced by decreasing the element spacing. However, reducing the element spacing will lead to an impedance mismatch between ports, which can be solved by changing the structure of the feed network and correctly using matching branches. The overall size change is shown in Figure 1.

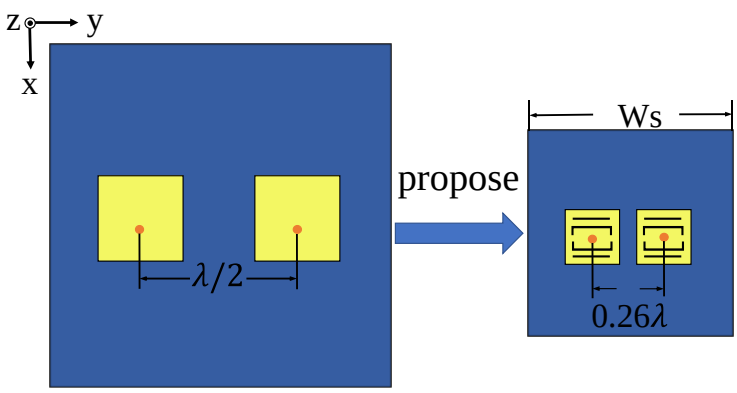

Figure 1. Comparison of antenna size between a conventional microstrip two-element array antenna and the proposed microstrip two-element array antenna.

The final antenna configuration comprises two slotted patches and a decoupled feed network, both of which are miniaturized, as shown in Figure 2. Its substrate is pressed using two layers of F4B (ε_r = 2.65, tanδ = 0.002) substrate, with a grounding layer between the two layers. The antenna unit is located on the top layer of the substrate, and U- and rectangular slots are added to it. The decoupling feed network is printed on the bottom layer of the substrate and is miniaturized by adding 12 branches. A matching branch is added to the external port to realize impedance matching with the external ports. A ground plane exists between the two substrates, and the feed network is fed to the two-element antenna array through the bottom feed. Two holes with a radius slightly larger than the coaxial line are introduced on the ground plane. The SMA connector is used as the feed launcher. All parameters of the antenna system are listed in Table 1.

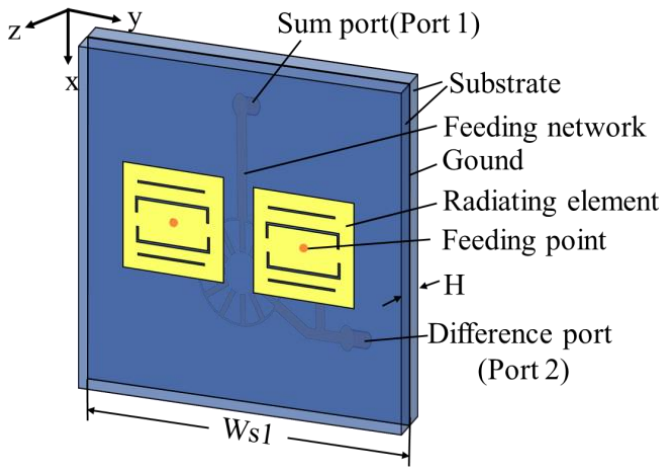

Figure 2. The designed mono-pulse antenna.

Table 1. Antenna parameters (unit: mm).

Para	Ws	d	W	v	v1	R	k1	k2	u
Value	78	32	23.4	17.1	16.5	3.8	6.1	8.4	0.3
Para	P	L1	L2	W1	W1s	R	R1	Wm	H
Value	11.2	23.15	11	2	1.5	4.3	11.1	0.3	1.48

2.2. Miniaturization Antenna

The relationship between microstrip antenna size and frequency is inversely proportional (here, the equation does not take into account the edge shortening effect), where W and L are the antenna length and width dimensions. The designed microstrip antenna operates in TM_{10} mode, and the antenna current path is shown in Figure 3. The equivalent current length of the slot is codirectional in the L direction and inverse in the W direction. The slot changes the direction of the current and lengthens the effective current path, thereby reducing the resonant frequency and miniaturizing the antenna.

$$W = \frac{c}{2f}\left(\frac{\varepsilon_r + 1}{2}\right)^{-\frac{1}{2}} \tag{1}$$

$$L = \frac{c}{2f\sqrt{\varepsilon_e}} \tag{2}$$

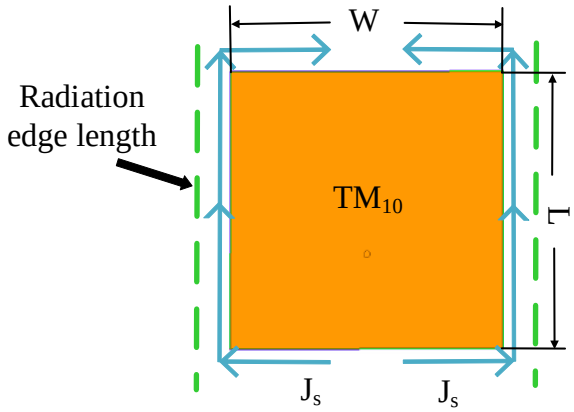

Figure 3. The current path of the microstrip antenna in TM_{10} mode.

In order to ensure that the shape of the antenna radiation pattern is not distorted, it is necessary to ensure that the slot is symmetrical along the *L* direction when the antenna surface is slotted, and the antenna current is still reversed in the *W* direction, with only the *L* direction component. The effect of slotting on the antenna path is shown in Figure 4. Comparing the three current distribution diagrams in Figure 4, the location of the maximum current is similar, but the path of the maximum current value in Figure 4b,c is longer, which indicates that it has the most significant effect of reducing the resonant frequency and the longest effective current path. The value of the current near the U-shaped slots is larger, so it plays the main role in extending the current path. When a U-shaped slot is added to the antenna, the resonant frequency is less than 8% of the bandwidth near the expected resonance point, and the *S* parameter is shown in Figure 5. Comparing Figure 4b,c, it can be seen that the function of the rectangular slot is to fine-tune the frequency to the resonant frequency point. The resonant frequency changes caused by the length of the slot and the size change of the microstrip antenna are shown in Figure 6. This is consistent with the above analysis indicating that the longer the antenna slot, the lower the resonant frequency.

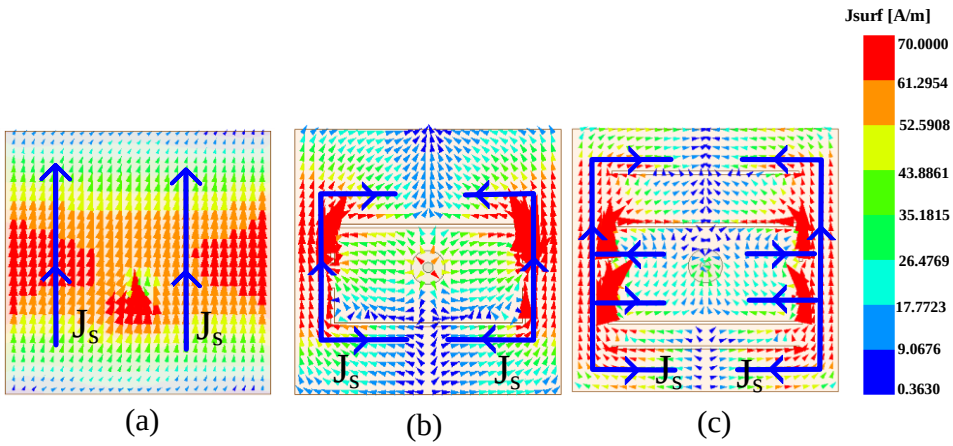

Figure 4. Effect of antenna slot on surface current path, and the arrows show the current direction. (**a**) Microstrip antenna's current distribution, (**b**) symmetric slots' current distribution, (**c**) two pairs of symmetric slots' current distribution.

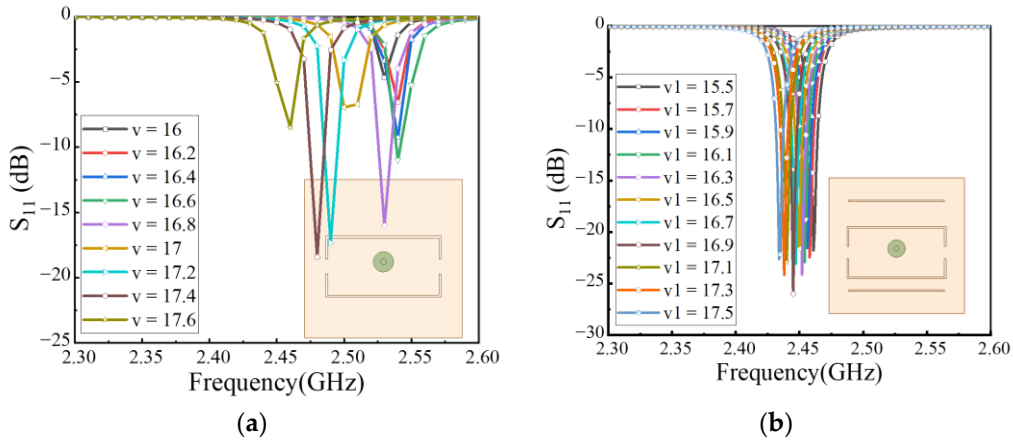

Figure 5. The slots to investigate the reflective characteristic. (**a**) Parameter v of U-shaped slots, (**b**) parameter v1 of rectangular slots.

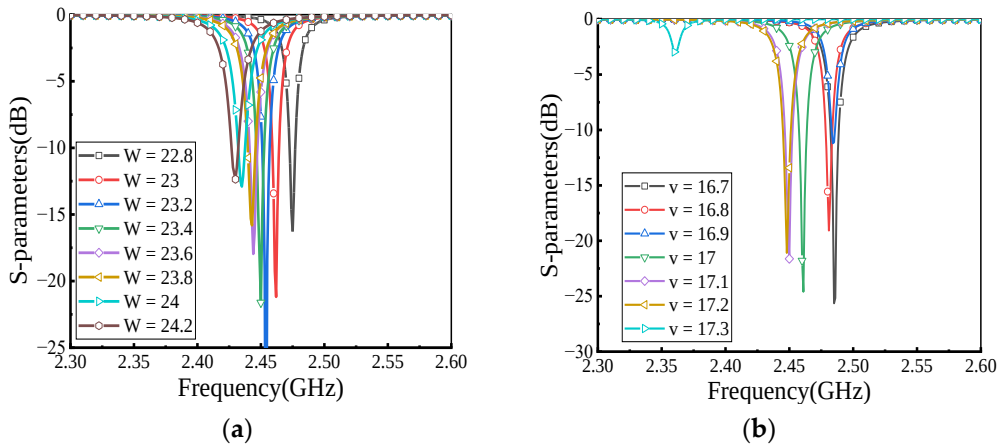

Figure 6. Effect of antenna size W and v on resonant point (unit: mm). (**a**) The antenna length parameter W, (**b**) parameter v1 of rectangular slots.

The feed point location in the antenna design process has some influence on the impedance matching. The input impedance of the microstrip antenna is affected by many parameters. For any feed point, the radiation resistance of the microstrip antenna is

$$R = \frac{45\pi^2\left\{\int_{-v/2-d}^{v/2-d}\left[\frac{1}{2\pi}\int_{-\infty}^{\infty} g(p)\frac{e^{-jpx}}{e^{|ph|}}dp\right]\cos\frac{\pi}{v}(x+d)dx\right\}^2}{\left(\frac{v}{\lambda_0}\right)^2\left[1-0.374\left(\frac{v}{\lambda_0}\right)^2+0.13\left(\frac{v}{\lambda_0}\right)^4\right]} \tag{3}$$

$$g(p) = \frac{\sin(pW_m/2)}{pW_2/2} - \frac{1}{2}\frac{\sin^2(pW_m/4)}{(pW_m/4)^4} \tag{4}$$

where the length of the slot is v, the distance from the feed point to the center of the slit is d, and p is a variable of the Fourier transform.

As shown in Figure 7, the position of the antenna feed point has a great influence on the impedance matching at the resonant frequency point, and the impedance matching can be better achieved by choosing the feed point position reasonably through formula calculation and simulation. When the feed-point position P = 11.2 mm, the S parameters of the antenna are optimized at the resonant frequency point.

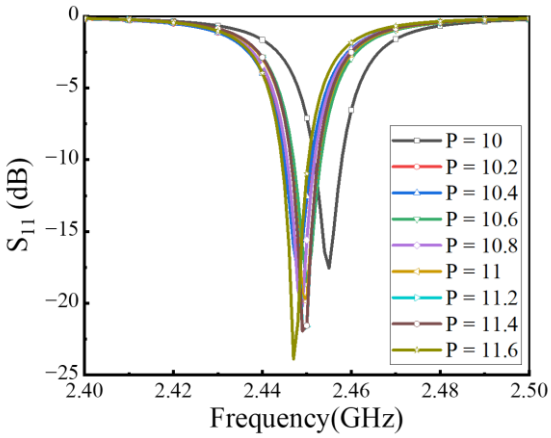

Figure 7. Effect of feed point location on resonant frequency.

The antenna has a frequency of 2.45 GHz. The miniaturized antenna unit was designed to be 23.4 × 23.4 mm^2 (0.19 λ × 0.19 λ), as shown in Figure 8. The *S* parameters and radiation patterns are shown in Figure 9.

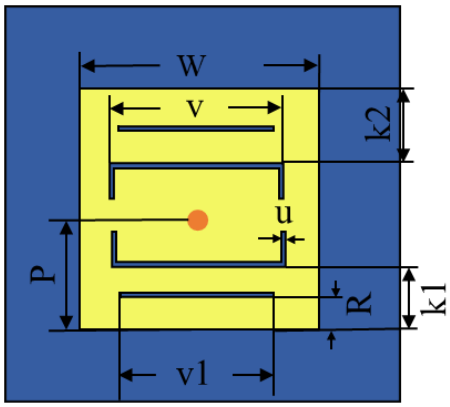

Figure 8. The miniaturized antenna.

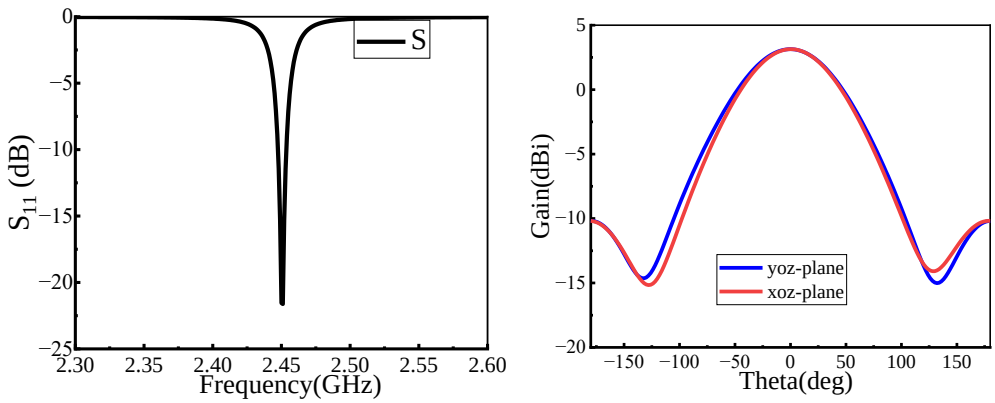

(a) (b)

Figure 9. Simulation results of miniaturization microstrip antenna unit. (**a**) S, (**b**) gain.

The addition of slots greatly reduces the size of the antenna unit. The final parameters were simulated and determined using ANSYS HFSS 2020R2 software. The simulation results of the miniaturized microstrip antenna are shown in Figure 8a,b. The S_{11} of the

antenna is greater than 21.6 dB, the antenna gain is 3.14 dBi, and the peak gain is at θ = 0°. The proposed antenna unit is approximately 59% smaller in size compared to previous versions. Compared with the two-element microstrip antenna (130 mm × 130 mm), the size of the designed antenna is reduced by 64%. The overall size change of the antenna is shown in Figure 1.

2.3. Decoupling Feed Network

Considering that the proposed mono-pulse antenna has two units, the feed network needs at least four ports, two for feeding the radiators and two for connecting the sum and difference ports, as shown in Figure 10. The electromagnetic wave at the external port is denoted by e, while *i* denotes the one at the internal port, and a and b denote the incident wave and the reflected wave, respectively.

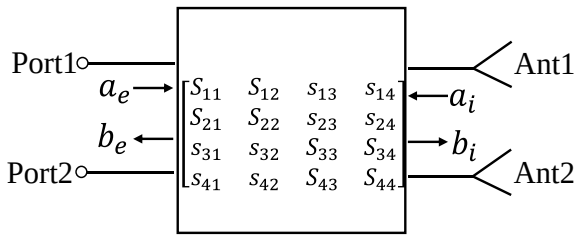

Figure 10. The feeding network scattering matrix.

The expression of the S parameter of the antenna feeding system is $b_e = S^a a_e$. When seen from the external port of the antenna feeding system, if the scattering matrix S is diagonal, it indicates that the antenna has been decoupled completely.

The scattering matrix expression of the array antenna can be formulated as follows

$$a_i = S^a b_i \tag{5}$$

The scattering matrix expression of the feeding network is

$$\begin{bmatrix} b_e \\ b_i \end{bmatrix} = \begin{bmatrix} S_{ee} & S_{ei} \\ S_{ie} & S_{ii} \end{bmatrix} \begin{bmatrix} a_e \\ a_i \end{bmatrix} \tag{6}$$

where a_i, b_i, a_e, and b_e are column vectors with two elements and S_{ee}, S_{ei}, S_{ie}, and S_{ii} are 2×2 matrices. For the ideal feed network, $S_{ee} = S_{ii} = 0$, $S_{ei} = {S_{ie}}^T$, then

$$b_e = S_{ei} S^a S_{ie} a_e = S^c a_e \tag{7}$$

Since the reflection coefficient of a mono-pulse antenna unit is small enough, it can be assumed that there is only coupling but no reflection between elements of the antenna array:

$$S^a = \begin{bmatrix} 0 & s_{12} \\ s_{21} & 0 \end{bmatrix}, \text{ and } s_{12} = s_{21}.$$

Through simple calculation, the eigenvectors can be obtained as

$$e_1 = \frac{1}{\sqrt{2}} \begin{bmatrix} 1 \\ 1 \end{bmatrix}, \; e_2 = \frac{1}{\sqrt{2}} \begin{bmatrix} 1 \\ -1 \end{bmatrix}.$$

The antenna array operates in the mode corresponding to the eigenvector e_1 with the feeds of both ports being of equal amplitude and in-phase and in the mode corresponding to e_2 with the feeds of both port being of equal amplitude and in-phase.

Therefore, $S_{ie} = [e_1 \quad e_2]$ and $S_{ei} = {S_{ie}}^T = S_{ie}^{-1}$. The scattering matrix of the antenna feeding system is diagonal. The two-element microstrip array antennas are decoupled.

The scattering matrix of the decoupled feeding network is

$$S^c = \begin{bmatrix} s_{11} & 0 & s_{13} & s_{13} \\ 0 & s_{22} & s_{14} & -s_{14} \\ s_{13} & s_{14} & s_{33} & s_{34} \\ s_{13} & -s_{14} & s_{34} & s_{44} \end{bmatrix}. \tag{8}$$

The decoupled network of the two-element microstrip array is obtained through matrix calculation, and the decoupled network can be represented by Figure 11.

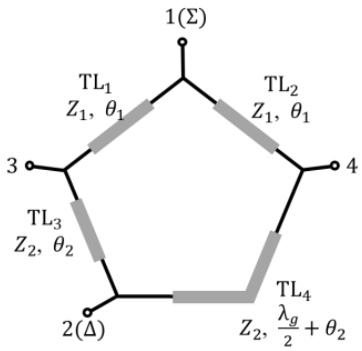

Figure 11. The transmission line equivalent model.

θ_1 and θ_2 take on arbitrary values. Figure 11 shows a common decoupling network for a two-element array of antennas.

In order to ensure that the decoupling network is better adapted to the miniaturized antenna array, take $\theta_1 = \theta_2 = \frac{\lambda_g}{8}$. TL_4 takes $\frac{\lambda_g}{4} + \theta_2$, and at this time, the decoupling network in the size of the ring is greatly reduced. However, changes in the size and impedance of the ring cause the imaginary part to arise. On the other hand, the phase at the difference port of the decoupling network cannot achieve reverse superposition. Therefore, an equivalent circuit is used to add an open short branch on the torus, as shown in Figure 12a,b. In this way, the impedance of the port can be matched. The phase-inverse superposition of differential ports is realized by adjusting the equivalent length of TL_4. The equivalent circuit is designed by adding an open branch, and the total size of the equivalent ring is $\frac{3\lambda_g}{2}$, and the corresponding transmission line impedance is $\sqrt{2}Z_0$. At this time, the impedance matching is realized at each port, and the phase inversion superposition is realized at the differential port.

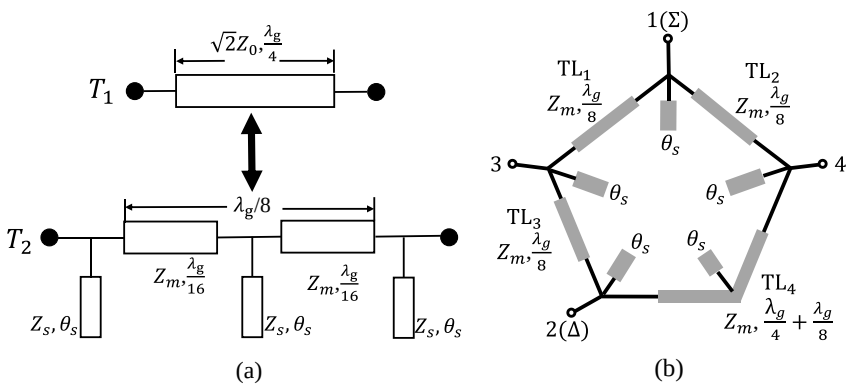

Figure 12. Equivalent circuit schematics. (**a**) Equivalent circuit of the transmission line; (**b**) equivalent schematic of the decoupling network.

The transmission (ABCD) matrix presented in Figure 11 is

$$T_1 = \begin{bmatrix} \cos\theta & jZ\sin\theta \\ jY\sin\theta & \cos\theta \end{bmatrix} \tag{9}$$

$$T_2 = \begin{bmatrix} 1 & 0 \\ jY_s\tan\theta_s & 1 \end{bmatrix} T_1 \begin{bmatrix} 1 & 0 \\ jY_s\tan\theta_s & 1 \end{bmatrix} T_1 \begin{bmatrix} 1 & 0 \\ jY_s\tan\theta_s & 1 \end{bmatrix} \tag{10}$$

For $T_1 = T_2$, the impedance of the transmission line and the open branch can be calculated as

$$Z_m = \frac{Z\sin\theta}{\sin\theta_m} \tag{11}$$

$$Z_s = \frac{Z\sin\theta\tan\theta_s}{\cos\theta_m - \cos\theta} \tag{12}$$

Considering the fabrication accuracy, the equivalent microstrip line cannot be fabricated and used if its width is less than 0.2 mm. Fixing the θ_s to 20°, the results of the final optimization parameters are recorded in Table 2, and the final feeding network model is shown in Figure 13.

Table 2. Equivalent model size.

Main Line				Equivalent Unit			
θ_m (°)	Z_m (Ω)	W_m (mm)	L_m (mm)	θ_s (°)	$Z_s/2$ (Ω)	W_s (mm)	L_s (mm)
22.5	130.6	0.24	5.5	20	42	2.58	4.55

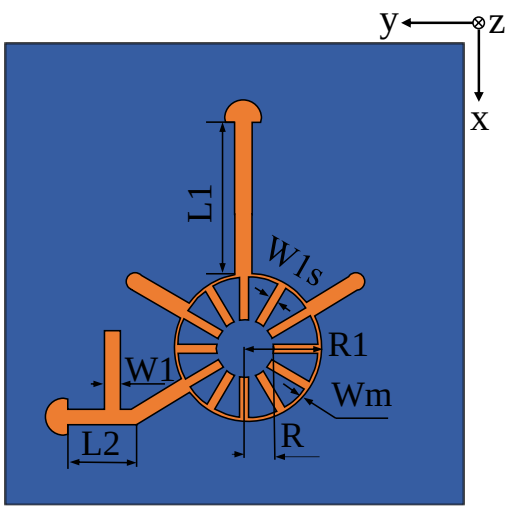

Figure 13. The structure of the miniaturization feed network.

As shown in Figure 14, the power fed to the network at 2.45 GHz has equal error in the two ports, at 0.1 dB, and the port isolation is greater than 25 dB.

We combine the two parts and match the external ports. The antenna model of the final design is shown in Figure 2. Figure 15 shows the changes in the S parameters of the antenna before and after decoupling. The reduction in S_{21} by about 30 dB after antenna decoupling indicates that the designed decoupling network can isolate the two outer ports well.

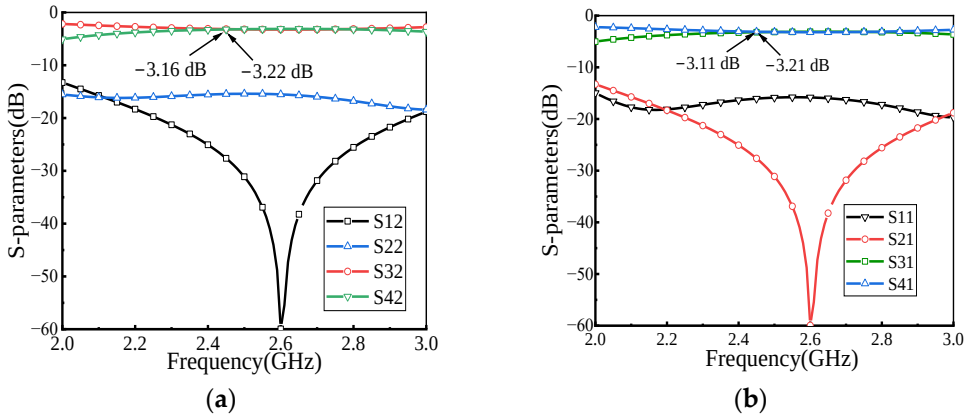

Figure 14. The feed network simulation results. (**a**) Sum port. (**b**) Difference port.

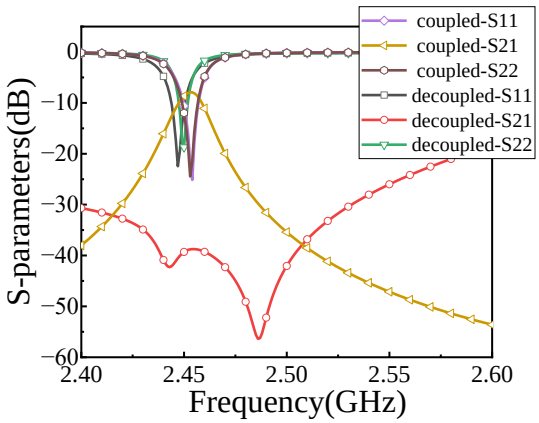

Figure 15. The difference in *S* parameters of the mono-pulse antenna before and after adding the decoupling network.

3. Result

The array antenna was connected to the feeding unit. The measured results are shown in Figure 16a,b. The measurement environment is shown in Figure 17. The *S* parameter test used Anritsu's vector network analyzer, which measured 201 points in the band 2.4–2.6 GHz. LB-10180-SF wideband horn antennas with a frequency of 1–18 GHZ were used for the measurement of antenna gain.

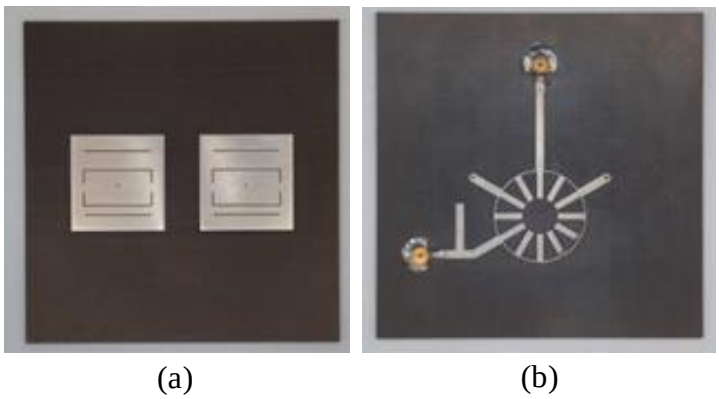

Figure 16. Antenna diagram. (**a**) The top surface. (**b**) The bottom surface.

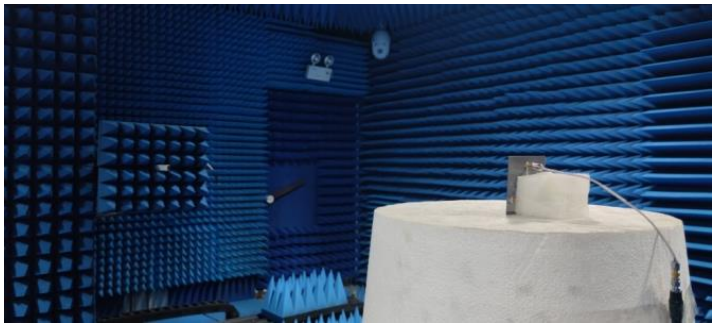

Figure 17. The antenna measurement environment.

The simulated *S* parameters are depicted in Figure 18, which shows a frequency discrepancy of 3 MHz in the reflection coefficient between the sum and difference ports. The simulation results show that the sum return loss is 16.14 dB, the difference return loss is 15.2 dB, and the isolation between ports is 36.6 dB. The measurement results show that the sum return loss is 14.7 dB, the difference return loss is 16.7 dB, and the isolation between ports is 28.3 dB.

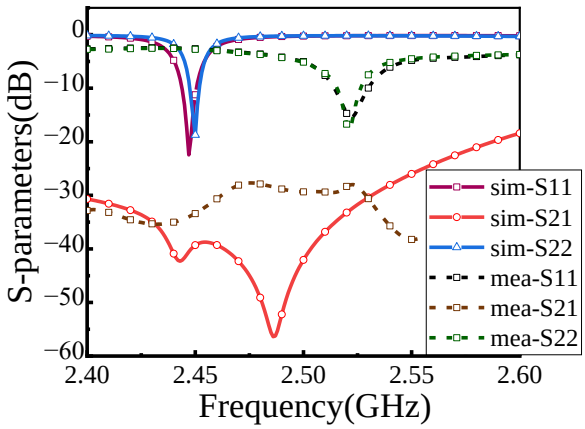

Figure 18. The antenna simulation and measurement results.

The proposed antenna is a one-dimensional sum and difference beamforming antenna, and the observed principal plane is the radiation pattern on the y–z plane. From Figure 19a,b, the measured and simulated results of the mono-pulse antenna fit well at the center frequency of 2.45 GHz.

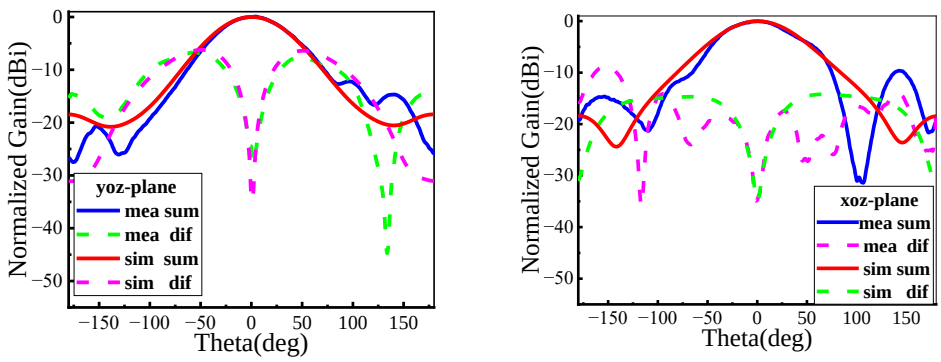

(**a**) (**b**)

Figure 19. Simulation and measured gain results of the antenna. (**a**,**b**) are radiation patterns.

When the antenna spacing is greater than 0.5 λ, the antennas have good isolation. Compared with the previous work, the designed antenna unit size is smaller, and the isolation between the two ports is good. Table 3 shows a comparison between the proposed work and previous research results.

Table 3. The comparison between the proposed design of compact decoupled antenna and previous work.

Ref.	Antenna Unit Size	Array Type	Array Spacing	10 dB Bandwidth (GHz)	Gain (dBi)	Isolation (dB)
[21]	0.98 λ × 0.7 λ	2 × 2	0.48 λ	7.9–9.59	8.3	>18
[22]	0.22 λ × 0.18 λ × 0.76 λ	5 × 6	0.22 λ	26.5–29.5	7	>23
[23]	1.03 λ × 0.59 λ × 0.05 λ	1 × 2	0.44 λ	5.12–6.32	5.8	≥20
[24]	0.33 λ × 0.5 λ	1 × 2	0.42 λ	2.39–2.57, 3.82–6.95	2.65	>15
[25]	1.58 λ × 0.75 λ × 0.024 λ	2 × 4	0.12 λ	4–5.4	3.6	>27
[26]	0.19 λ × 0.21 λ	1 × 4	0.48 λ	5.49–6.024	5.34	>33
[27]	0.316 λ × 0.316 λ	4 × 4	0.5 λ	2.4–2.485	7	>25
Proposed	0.19 λ × 0.19 λ	1 × 2	0.27 λ	2.4453–2.4533	5.54	>36.6

4. Conclusions

The measured results are shown in Figure 18. The difference between the measured value of the *S* parameter (2.52 GHz) and the simulation result (2.45 GHz) is 0.07 GHz. There are two reasons for the discrepancy between the measured results and the simulated results. One of these reasons is the imbalance in the power distribution of the feed network. When measured, it is difficult to make the output current of the two ports exactly the same. Another reason is the fluctuation of the relative permittivity of the fabricated substrate, leading to a deviation in the measured and simulated center frequency. These factors can contribute to the differences observed in the performance of the antenna. However, it is worth noting that the miniaturization of the antenna did not hardly affect its radiation patterns. The measured results are in good agreement with the simulated results in terms of electrical performance.

The miniaturization of mono-pulse antennas through the design of miniaturized radiating units and reduced spacing between dual-element antenna arrays exhibits promising prospects for various applications. This approach enables the maintenance of unchanged electrical characteristics after miniaturization by decoupling the operation. It effectively reduces the size of sum and difference antennas while ensuring good electrical performance. Moreover, this method can be extended to two-dimensional mono-pulse antennas and miniaturized antenna arrays.

Author Contributions: Conceptualization, Z.W. and D.Y.; methodology, Z.W.; software, K.X.; validation, Z.W., D.Y. and K.X.; formal analysis, K.X.; investigation, D.Y.; resources, Z.W.; data curation, Z.W.; writing—original draft preparation, D.Y.; writing—review and editing, K.X.; visualization, Z.W.; supervision, Z.W.; project administration, K.X.; funding acquisition, D.Y. All authors have read and agreed to the published version of the manuscript.

Funding: This research received no external funding.

Data Availability Statement: No applicable.

Conflicts of Interest: The authors declare no conflict of interest.

References

1. Gao, X.; Roy, S.; Xing, G. MIMO-SAR: A Hierarchical High-Resolution Imaging Algorithm for mmWave FMCW Radar in Autonomous Driving. *IEEE Trans. Veh. Technol.* **2021**, *70*, 7322–7334. [CrossRef]
2. Mei, P.; Zhang, Y.-M.; Zhang, S. Decoupling of a Wideband Dual-Polarized Large-Scale Antenna Array with Dielectric Stubs. *IEEE Trans. Veh. Technol.* **2021**, *70*, 7363–7374. [CrossRef]
3. Kerketta, S.R.; Ghosh, D. Gain Enhancement of Extremely Wide Band Stubbed Monopole Antenna Backed by Dielectric. In Proceedings of the 2019 IEEE 16th India Council International Conference (INDICON), Rajkot, India, 13–15 December 2019; pp. 1–3.
4. Zhang, S.; Pedersen, G.F. Mutual Coupling Reduction for UWB MIMO Antennas with a Wideband Neutralization Line. *IEEE Antennas Wirel. Propag. Lett.* **2016**, *15*, 166–169. [CrossRef]
5. Zhang, L.; Lin, L.; Zhang, L.; Wang, Y. A 150GHz amplifier based on coupled transmission line neutralization and inter stage impedance matching with 20dB gain in 65nm CMOS. In Proceedings of the 2017 International Conference on Electron Devices and Solid-State Circuits (EDSSC), Hsinchu, Taiwan, 18–20 October 2017; pp. 1–2.
6. Tang, X.; Mouthaan, K.; Coetzee, J.C. Tunable Decoupling and Matching Network for Diversity Enhancement of Closely Spaced Antennas. *IEEE Antennas Wirel. Propag. Lett.* **2012**, *11*, 268–271. [CrossRef]
7. Ping, T.C.; Coetzee, J.C. Microstrip decoupling networks for low-order multiport arrays with reduced element spacing. *Microw. Opt. Technol. Lett.* **2010**, *46*, 592–597.
8. Zhang, Y.-M.; Ye, Q.-C.; Pedersen, G.F.; Zhang, S. A Simple Decoupling Network with Filtering Response for Patch Antenna Arrays. *IEEE Trans. Antennas Propag.* **2021**, *69*, 7427–7439. [CrossRef]
9. Li, Y.; Chu, Q.-X. Self-Decoupled Dual-Band Shared-Aperture Base Station Antenna Array. *IEEE Trans. Antennas Propag.* **2022**, *70*, 6024–6029. [CrossRef]
10. Boroujeni, S.R.; Safavi-Naeini, S. A Broadband H-Plane Patch Antenna Decoupling Technique. In Proceedings of the 2019 IEEE International Symposium on Antennas and Propagation and USNC-URSI Radio Science Meeting, Atlanta, GA, USA, 31 October 2019; pp. 1763–1764.
11. Chen, J.; Han, L.; Yang, R.; Zhang, W. Design of a Slot Antenna Array Using Array-antenna Decoupling Surface. In Proceedings of the 2019 Cross Strait Quad-Regional Radio Science and Wireless Technology Conference (CSQRWC), Taiyuan, China, 18–21 July 2019; pp. 1–3.
12. Lin, L.-X.; Tu, Z.-H.; Zhu, H. Isolation Enhancement in Millimeter-wave MIMO Array Base on Array-Antenna Decoupling Surface. In Proceedings of the 2022 IEEE MTT-S International Microwave Workshop Series on Advanced Materials and Processes for RF and THz Applications (IMWS-AMP), Guangzhou, China, 27–29 November 2022; pp. 1–3.
13. Li, J.; Zhang, A.; Joines, W.T.; Liu, Q.H. A miniaturized circularly polarized microstrip antenna with bandwidth enhancement. In Proceedings of the 2016 IEEE International Symposium on Antennas and Propagation (APSURSI), Fajardo, PR, USA, 26 June–1 July 2016; pp. 41–42.
14. Asahina, I.; Saito, S.; Kimura, Y. Resonant Frequency Control of a Varactor-Loaded Single-Layer Triple-Band Miniaturized Microstrip Antenna Fed by an L-probe with Straight Shorted Elements. In Proceedings of the 2022 IEEE International Workshop on Electromagnetics: Applications and Student Innovation Competition (iWEM), Narashino, Japan, 29–31 August 2022; pp. 142–143.
15. Wu, J.; Ren, X.; Wang, Z.; Yin, Y. Broadband Circularly Polarized Antenna with L-shaped Strip Feeding and Shorting-Pin Loading. *IEEE Antennas Wirel. Propag. Lett.* **2014**, *13*, 1733–1736. [CrossRef]
16. Chen, X.; Zhao, M.; Huang, H.; Wang, Y.; Zhu, S.; Zhang, C.; Yi, J.; Kishk, A.A. Simultaneous Decoupling and Decorrelation Scheme of MIMO Arrays. *IEEE Trans. Veh. Technol.* **2022**, *71*, 2164–2169. [CrossRef]
17. Peng, Z.; Zhou, J.; Rao, Y.; Deng, Z.; Luo, X. Compact Bandpass Filter with Wide Stopband and Low Radiation Using Fully-Packaged Substrate Integrated Defected Ground Structure. In Proceedings of the 2021 IEEE International Symposium on Radio-Frequency Integration Technology (RFIT), Hualien, Taiwan, 25–27 August 2021; pp. 1–3.
18. Nasimuddin; Qing, X.; Chen, Z.N. A Compact Circularly Polarized Slotted Patch Antenna for GNSS Applications. *IEEE Trans. Antennas Propag.* **2014**, *62*, 6506–6509. [CrossRef]
19. Batel, L.; Pintos, J.-F.; Delaveaud, C. Design of a monopolar wire-plate antenna loaded with magneto-dielectric material. In Proceedings of the 12th European Conference on Antennas and Propagation (EuCAP 2018), London, UK, 9–13 April 2018; pp. 1–5.
20. Yang, M.; Chen, Z.N.; Lau, P.Y.; Qing, X.; Yin, X. Miniaturized Patch Antenna with Grounded Strips. *IEEE Trans. Antennas Propag.* **2015**, *63*, 843–848. [CrossRef]
21. Kulkarni, J.; Sim, C.-Y.-D.; Garner, B.; Li, Y. A Dual CP Quad-Port MIMO Antenna with Reduced Mutual Coupling for X-band Application. *IEEE Antennas Wirel. Propag. Lett.* **2023**, *22*, 2085–2089. [CrossRef]
22. Shen, X.; Liu, Y.; Zhao, L.; Huang, G.-L.; Shi, X.; Huang, Q. A Miniaturized Microstrip Antenna Array at 5G Millimeter-Wave Band. *IEEE Antennas Wirel. Propag. Lett.* **2019**, *18*, 1671–1675. [CrossRef]
23. Tran, H.H.; Hussain, N.; Le, T.T. Low-profile wideband circularly polarized MIMO antenna with polarization diversity for WLAN applications. *AEU-Int. J. Electron. Commun.* **2019**, *108*, 172–180. [CrossRef]
24. Sim, C.-Y.-D.; Dhasarathan, V.; Tran, T.K.; Kulkarni, J.; Garner, B.A.; Li, Y. Mutual Coupling Reduction in Dual-Band MIMO Antenna Using Parasitic Dollar-Shaped Structure for Modern Wireless Communication. *IEEE Access* **2023**, *11*, 5617–5628. [CrossRef]

25. Chaudhuri, S.; Kshetrimayum, R.S.; Sonkar, R.K. High inter-port isolation dual circularly polarized slot antenna with split-ring resonator based novel metasurface. *AEU Arch. Elektron. Übertrag. Electron. Commun.* **2019**, *107*, 146–156. [CrossRef]
26. Malviya, L.; Panigrahi, R.K.; Kartikeyan, M. Circularly polarized 2 × 2 MIMO antenna for WLAN applications. *Prog. Electromagn. Res. C* **2016**, *66*, 97–107. [CrossRef]
27. Zhang, E.; Michel, A.; Pino, M.R.; Nepa, P.; Qiu, J. A Dual Circularly Polarized Patch Antenna with High Isolation for MIMO WLAN Applications. *IEEE Access* **2020**, *8*, 117833–117840. [CrossRef]